Fig. 1: An event display from Milagrito. The length of each vertical line is proportional to the time at which that PMT was struck by light produced by particles in the shower front. This illustrates how the PMT signal times are used to reconstruct the direction of an air shower.

Fig. 2: Aerial photograph of the Milagrito site. The pond that housed Milagrito was empty when this photograph was taken. The utility building and electronics trailer are visible immediately to the left of the pond.

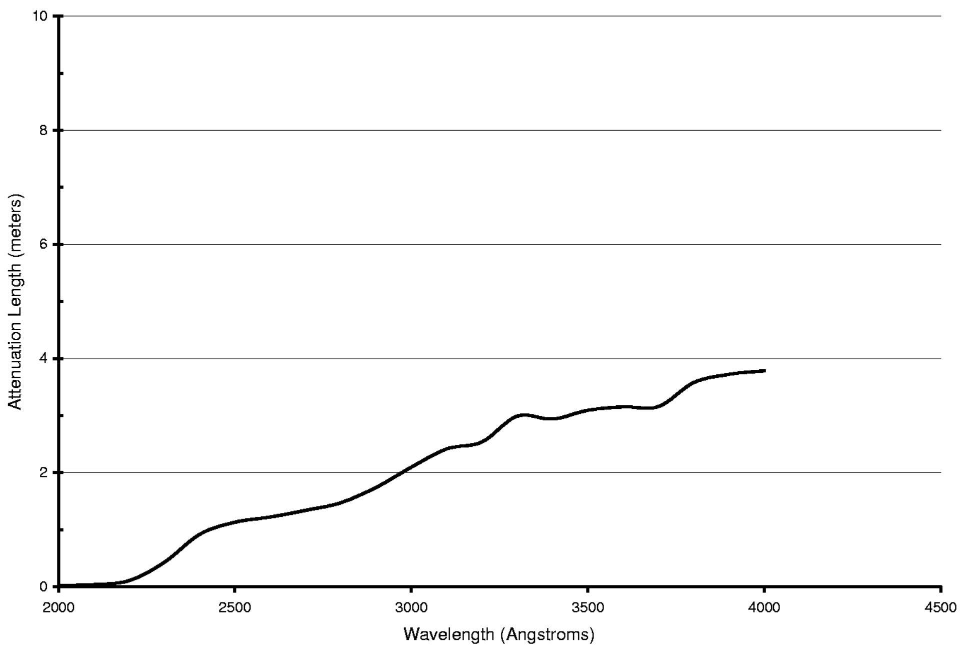


Fig. 3: The attenuation length vs. wavelength of the water in the Milagrito pond.

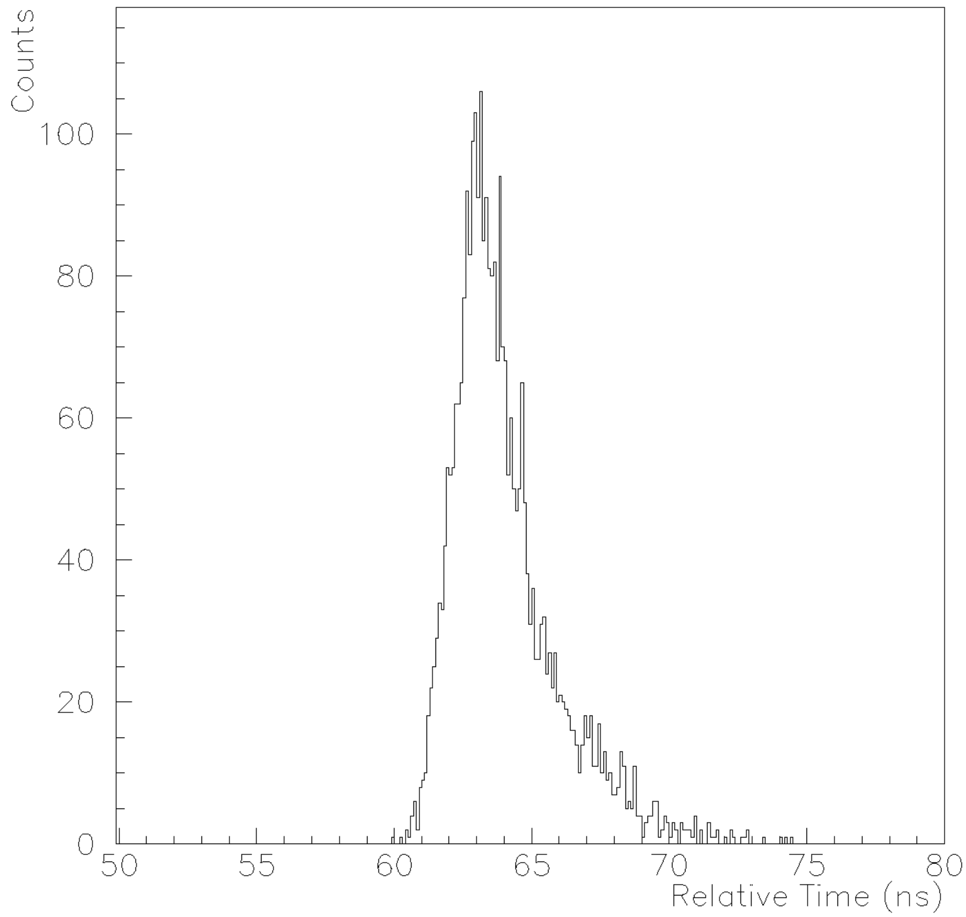


Fig. 4: The time response for single photoelectrons for a typical Hamamatsu R5912SEL photomultiplier operating at a gain of ~$10^7$.

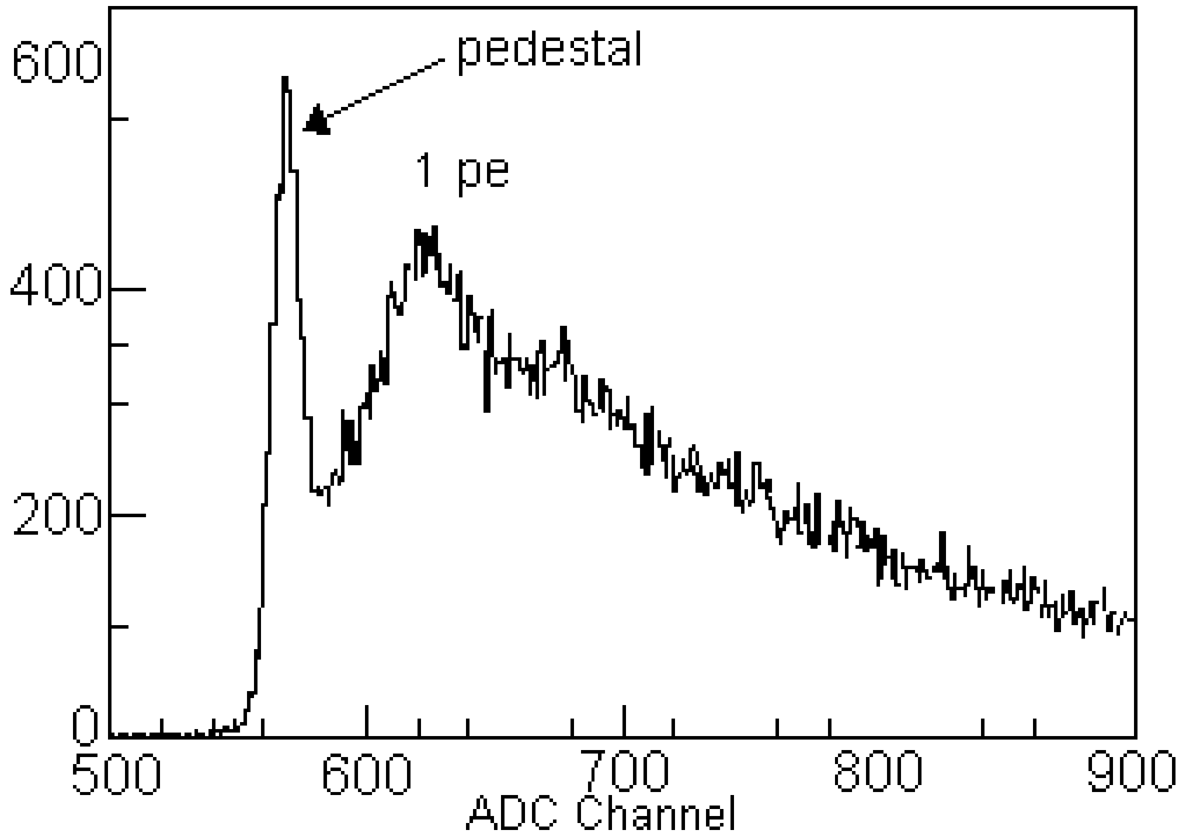


Fig. 5: The measured pulse charge spectrum for a typical Hamamatsu R5912SEL photomultiplier showing the ADC pedestal (channel ~570) and the single photoelectron peak (channel ~625).

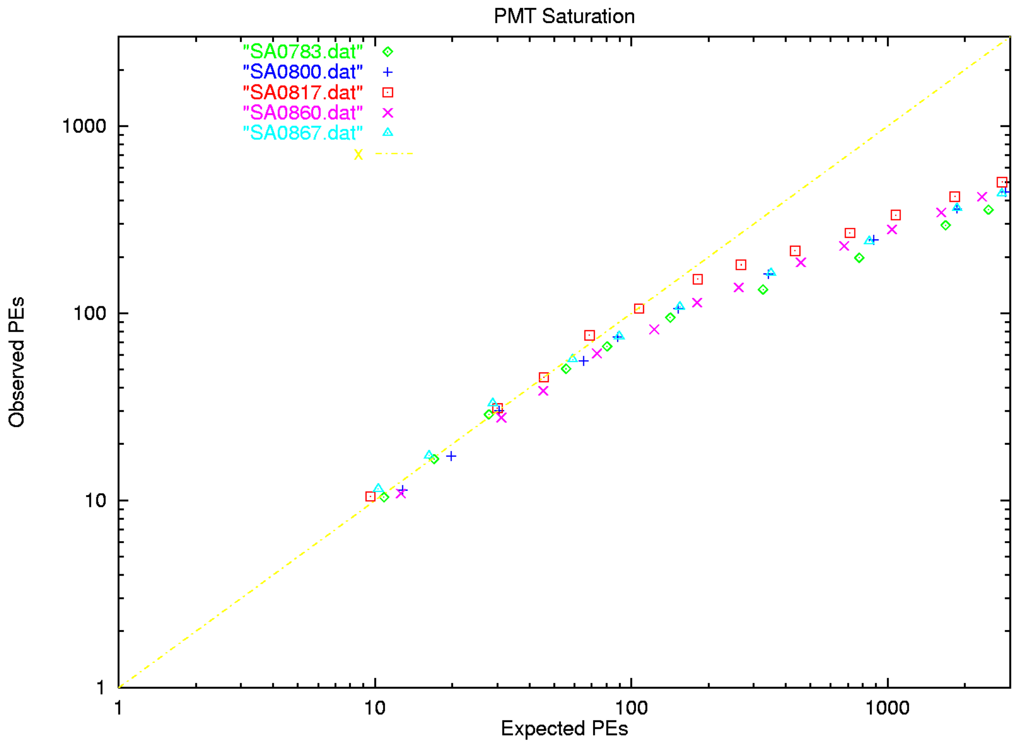


Fig. 6: The observed number of photoelectrons vs. the expected number for 5 Hamamatsu R5912SEL photomultipliers as measured with a pulsed laser and various attenuating filters.

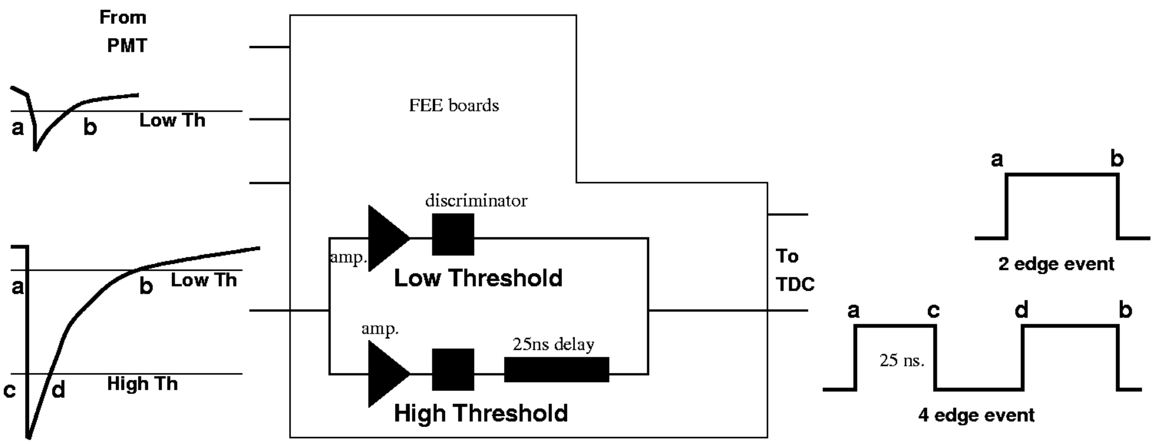


Fig. 7: A conceptual drawing of the dual TOT method illustrating the single logic pulse produced for an analog pulse that triggers only the low threshold, and the two pulses separated by the high TOT for a pulse that triggers the high threshold.

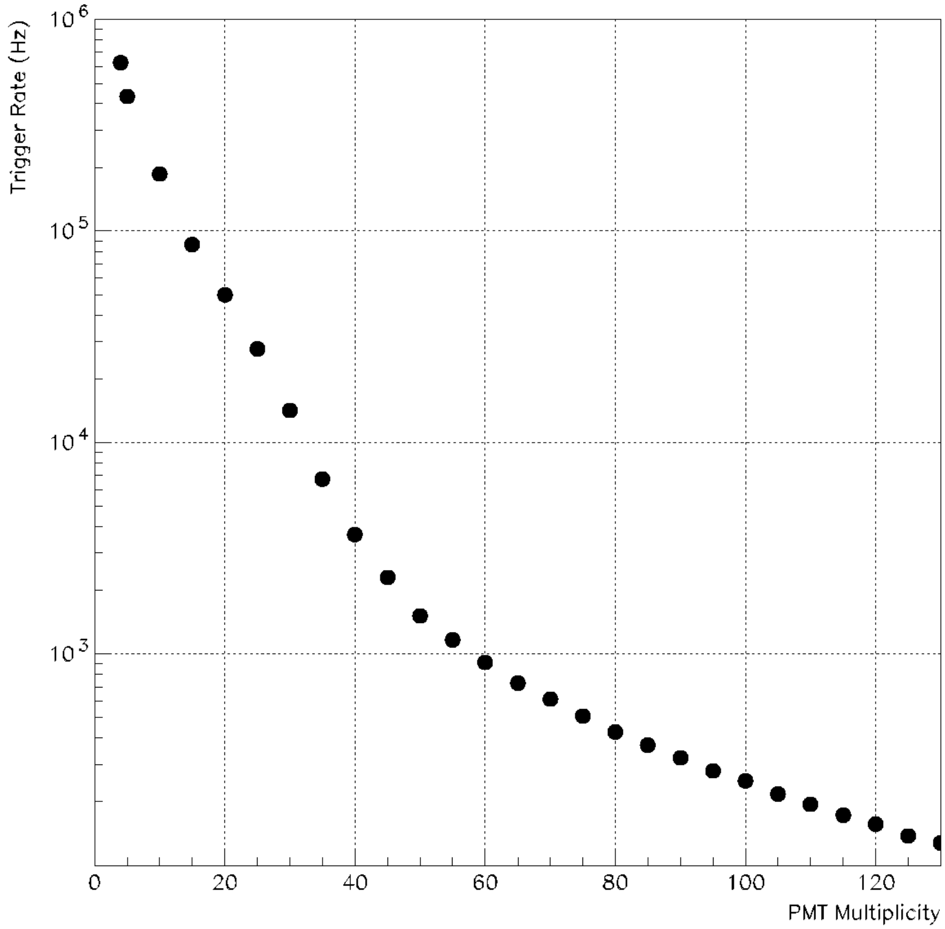


Fig. 8: The trigger rate vs. number of PMTs required in coincidence for a water depth of 1 m.

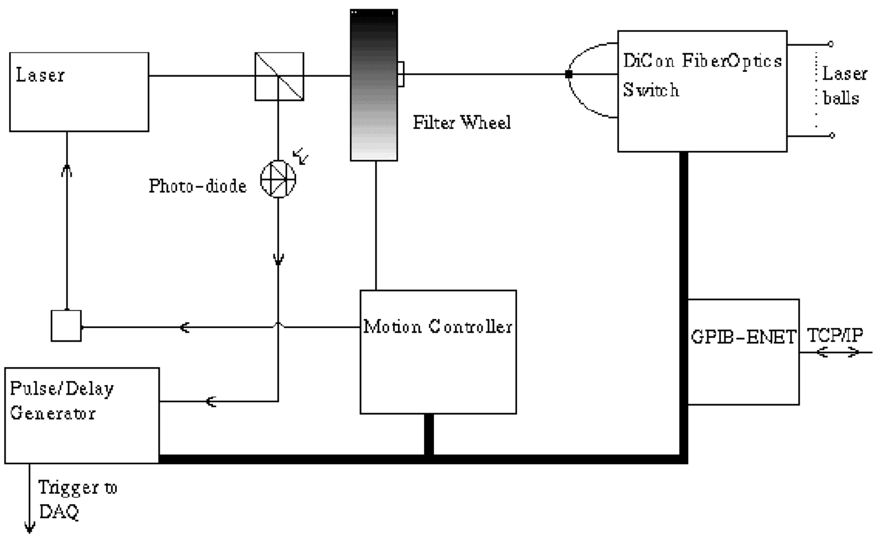


Fig. 9: A block diagram of the major components of the laser calibration system.

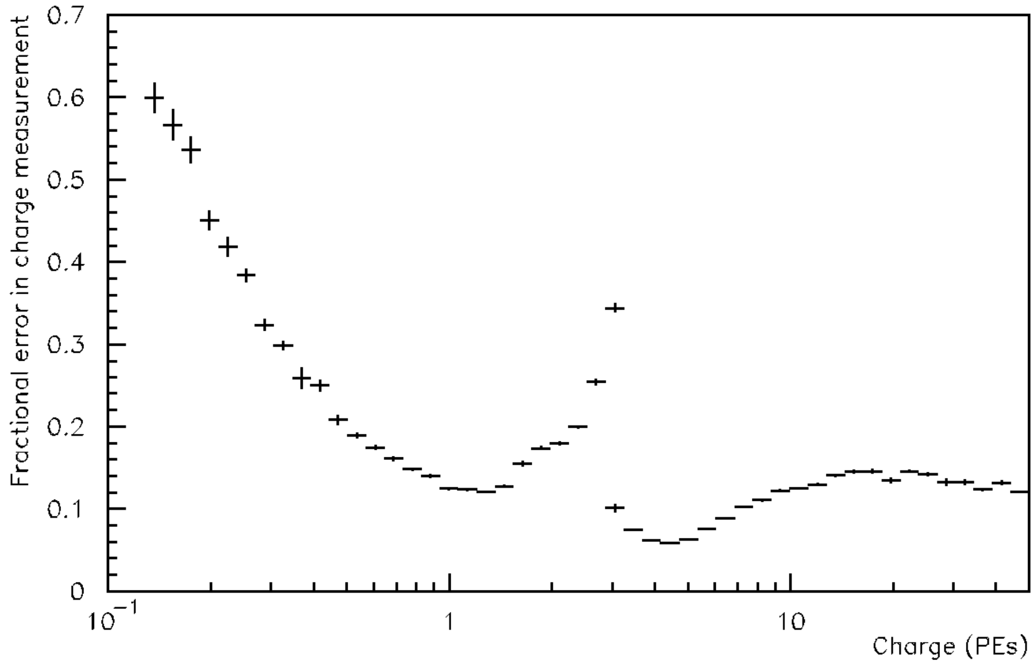


Fig. 10: The fractional error in the charge measurement as a function of charge (in units of PEs). The discontinuity near 3 PEs is due to the transition between the use of the low and high-threshold TOT measurements.

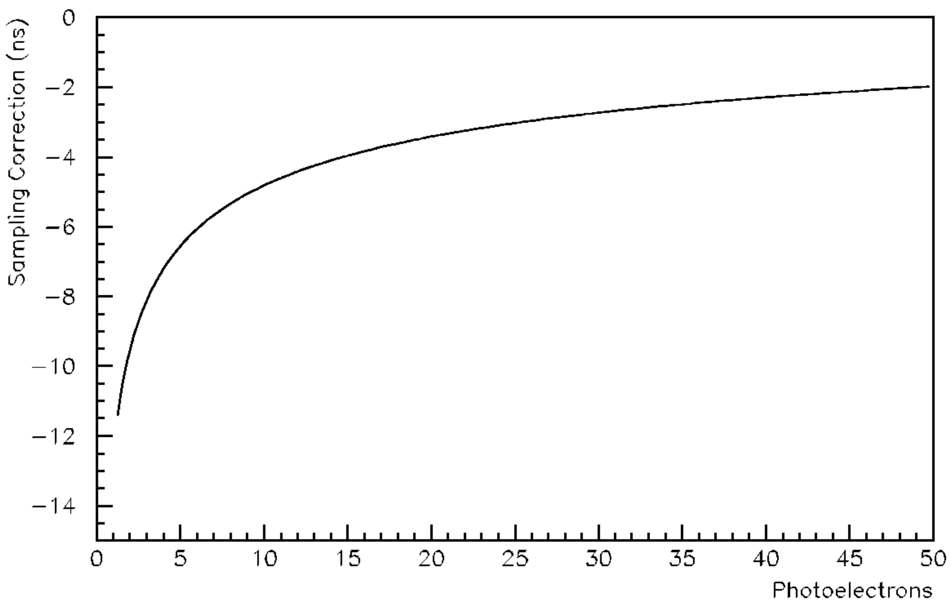


Fig. 11: The sampling correction as a function of the pulse height in a PMT.

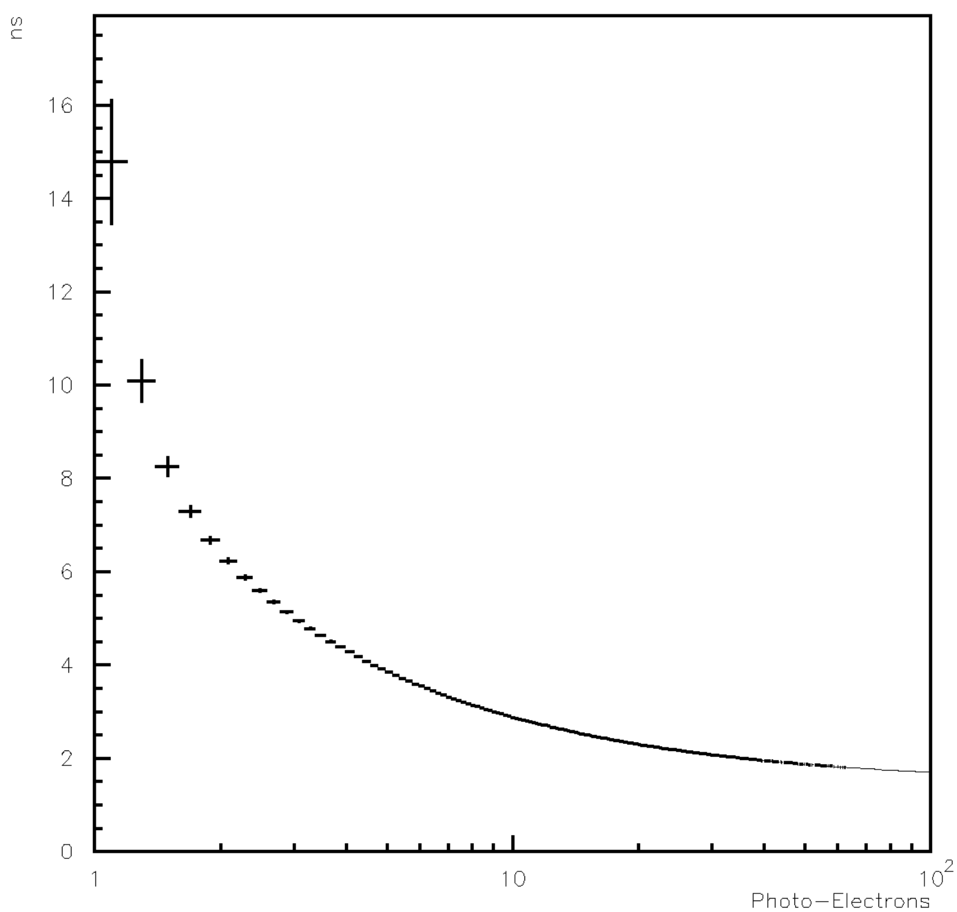


Fig. 12: The RMS timing resolution as a function of the number of detected photoelectrons in a PMT.

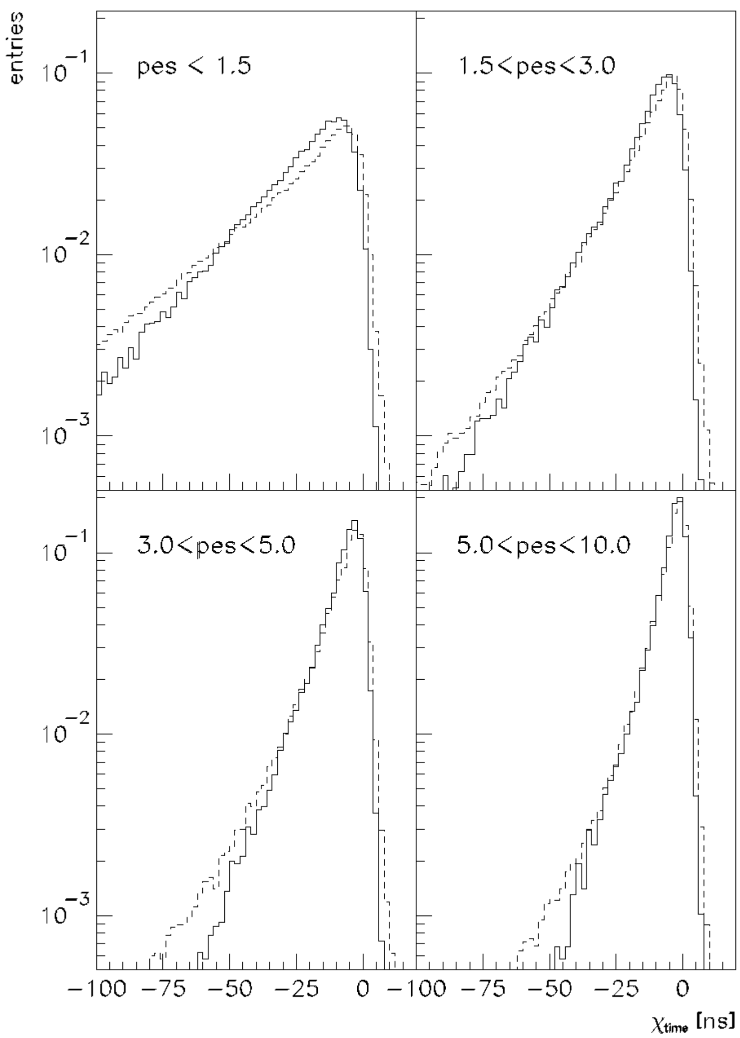


Fig. 13: The difference between the measured PMT time and the shower plane, $\chi_t$, for PMTs with the number of detected photoelectrons between 0 - 1.5, 1.5 -3, 3 - 5, and 5 - 10, for experimental data (dotted line) and simulated data (solid line).

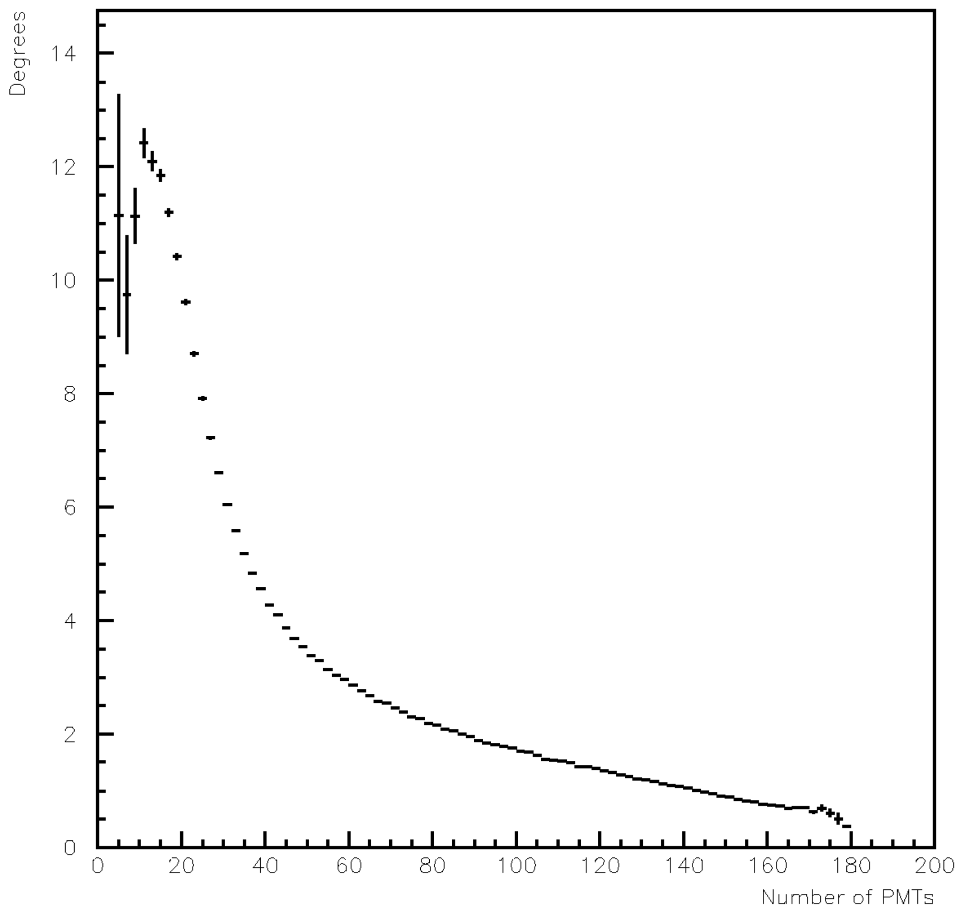


Fig. 14: The mean value of $\Delta_{EO}$ vs. the number of PMTs used in the fit, $N_{Fit}$, for data taken with a water depth of 2 m.

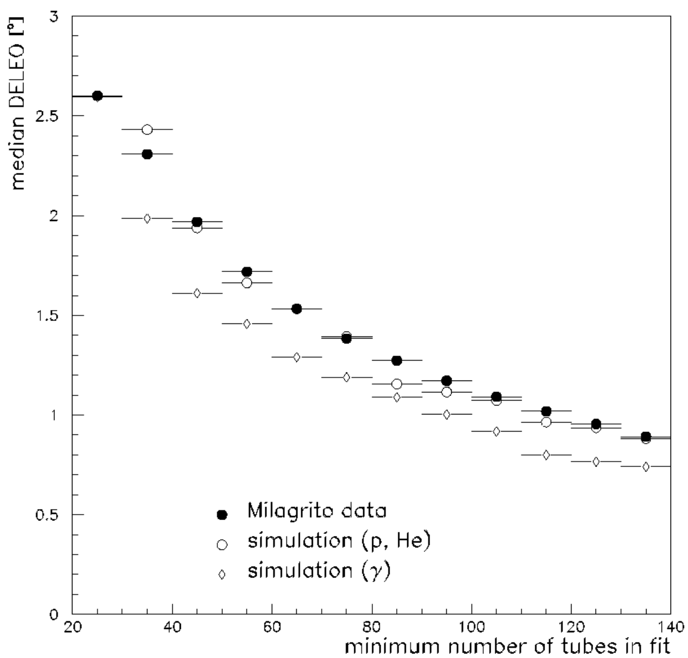


Fig. 15: The median value of $\Delta_{EO}$ vs. $N_{Fit}$ for data (with a water depth of 1 m) and Monte Carlo simulations.

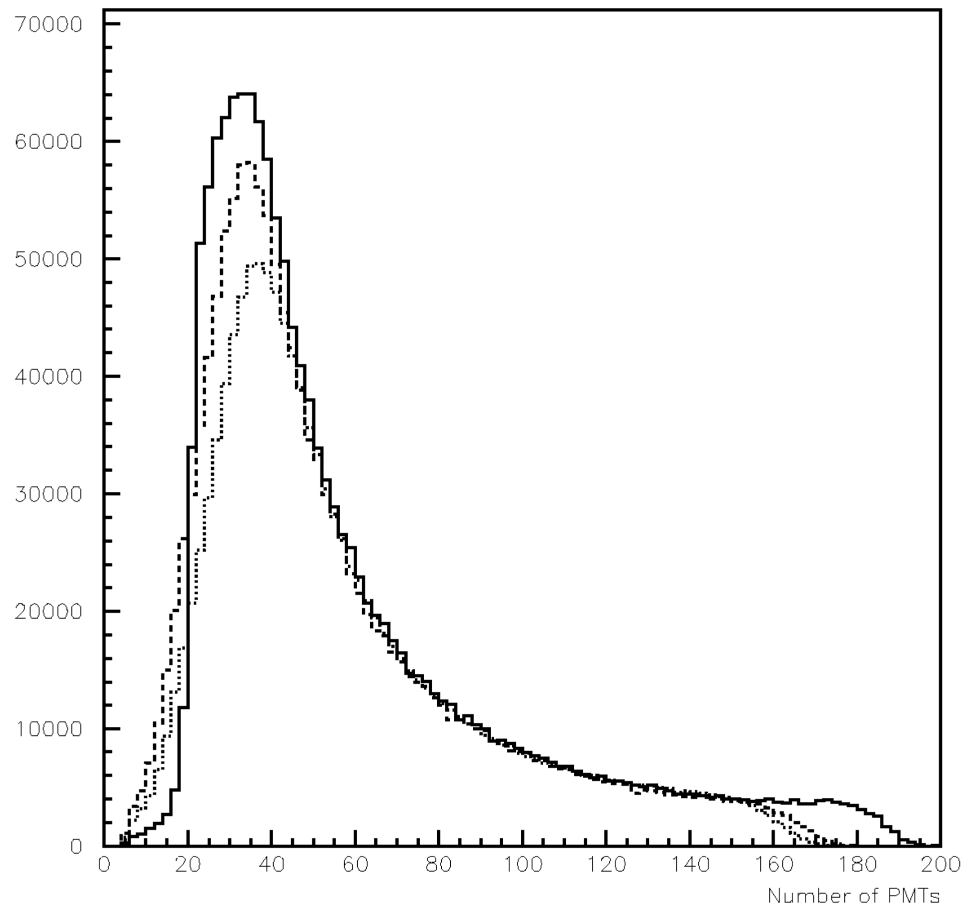


Fig. 16: The distribution of the number of events vs. $N_{Fit}$ for water depths of 1 m (solid histogram), 1.5 m of water (dashed histogram), and 2 m of water (dotted histogram). The three histograms are normalized to have the same areas. Note that the number of working PMTs is higher for the 1-m data.

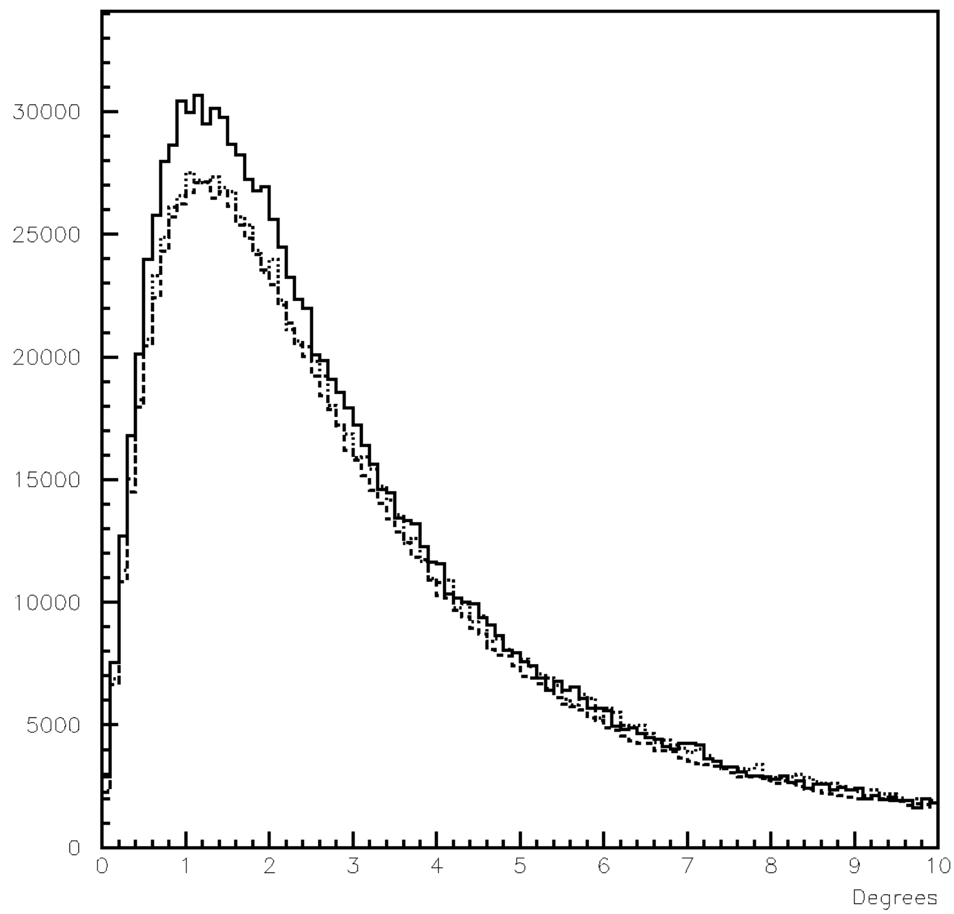


Fig. 17: The distribution of $\Delta_{EO}$ for events with $N_{Fit} \geq 40$ for the three different water depths. The dashed histogram is for 1 m, the solid is for 1.5 m, and the dotted is for 2 m. Note that the three histograms are normalized to have the same areas.

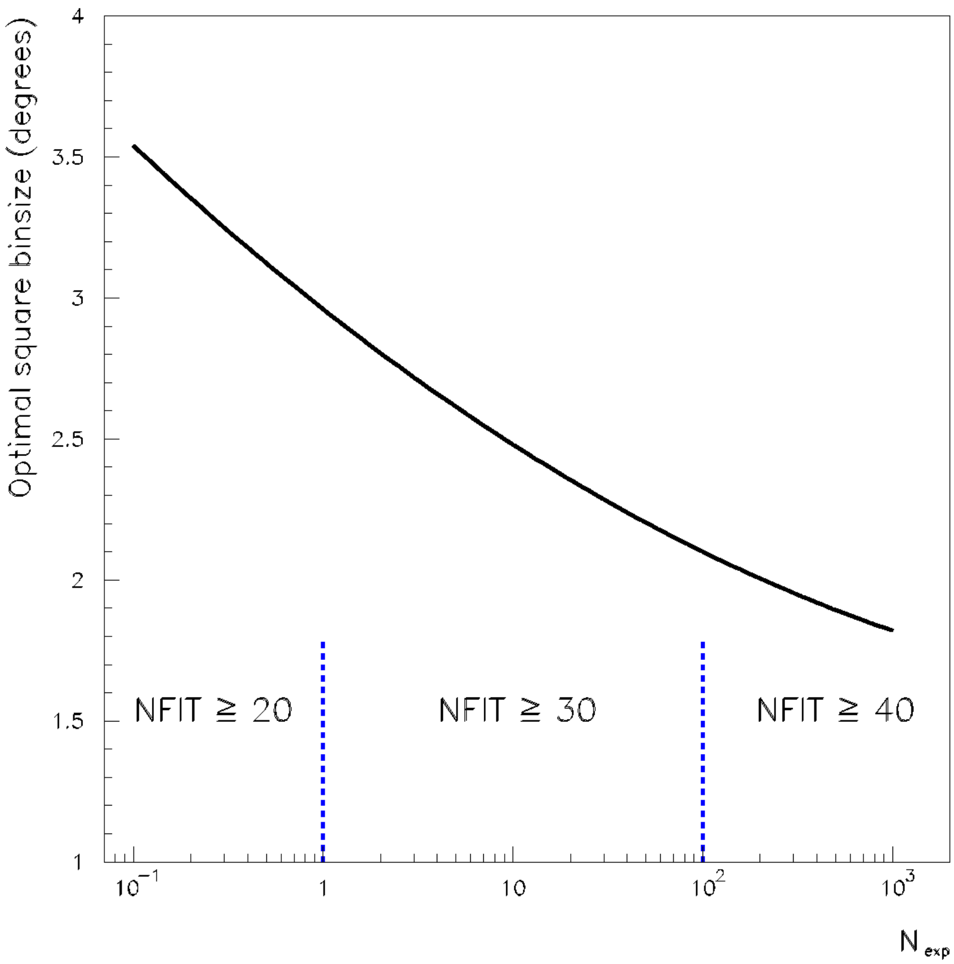


Fig. 18: The optimal bin size as a function of the expected number of background events in a 2° x 2° bin on the sky for data with 1 m of water. The figure also indicates the best cut on $N_{Fit}$ as a function of the expected number of background events in this bin.

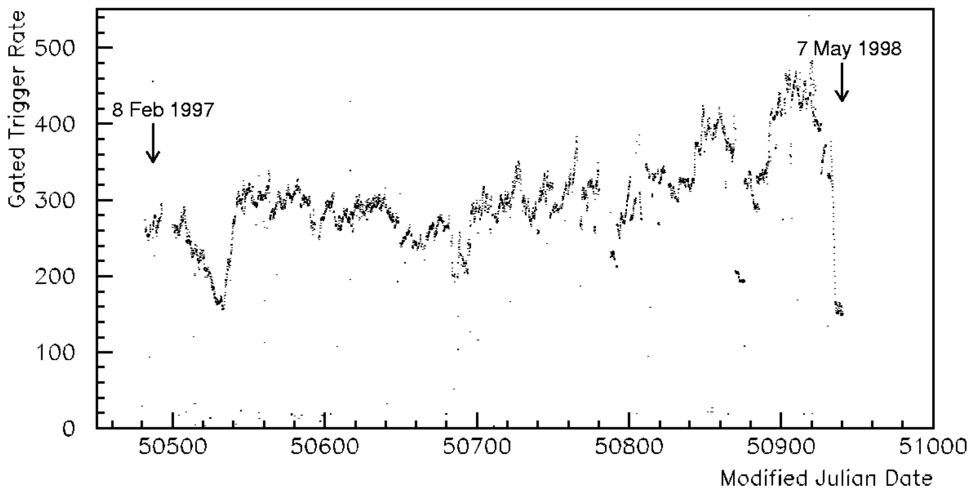


Fig. 19: The average daily event rate over the operating life of Milagrito.

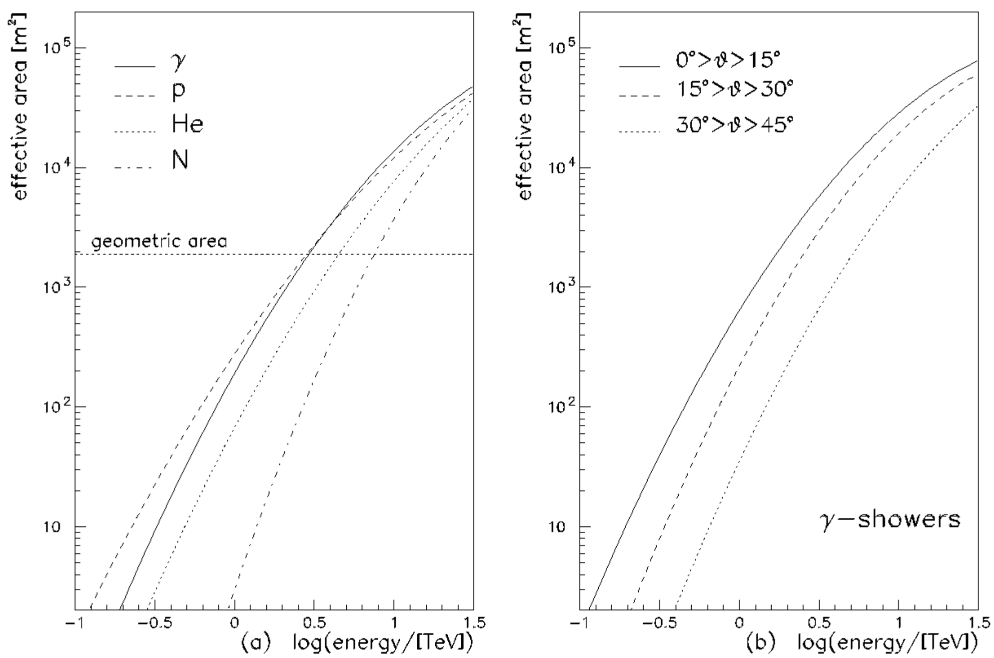


Fig. 20: (a) The effective area, $A_{eff}$, as a function of the energy of the primary particle for hadron and photon showers.

(b) Dependence of $A_{eff}$ with zenith angle.

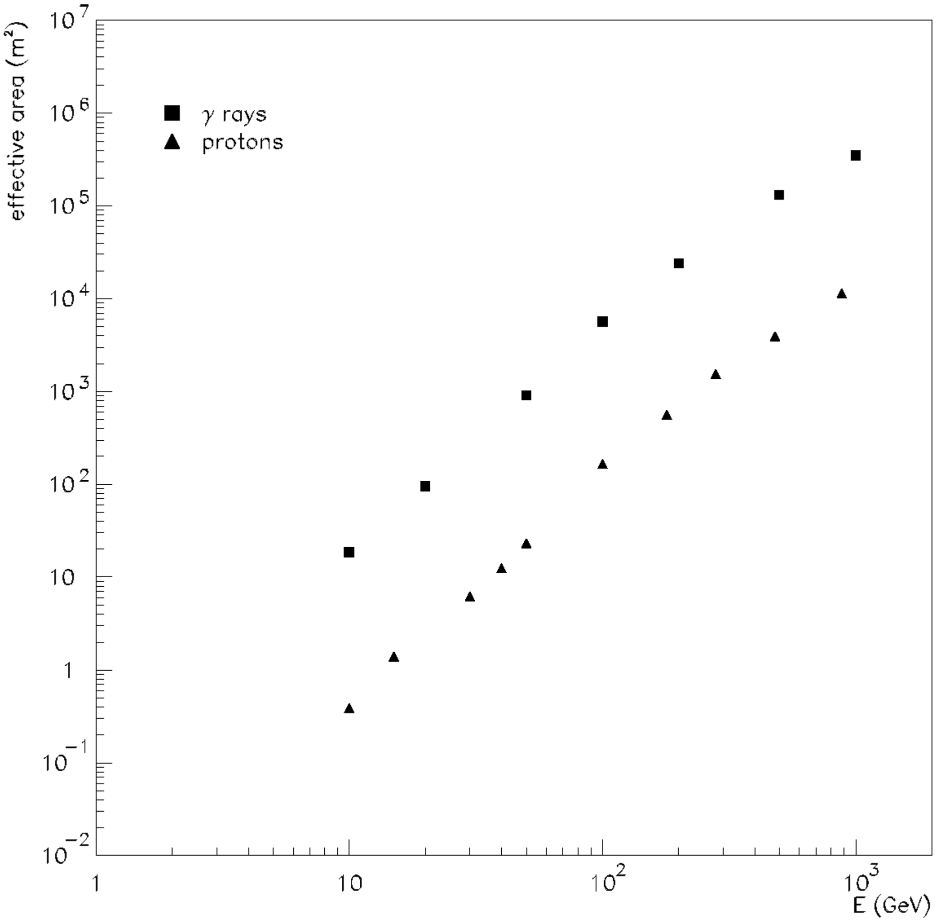


Fig. 21: The effective area as a function of energy for the scaler system. The squares are for cosmic gamma rays incident at a fixed zenith angle of 22°and the low-threshold scalers: the triangles are for isotropic cosmic protons and the high-threshold scalers.

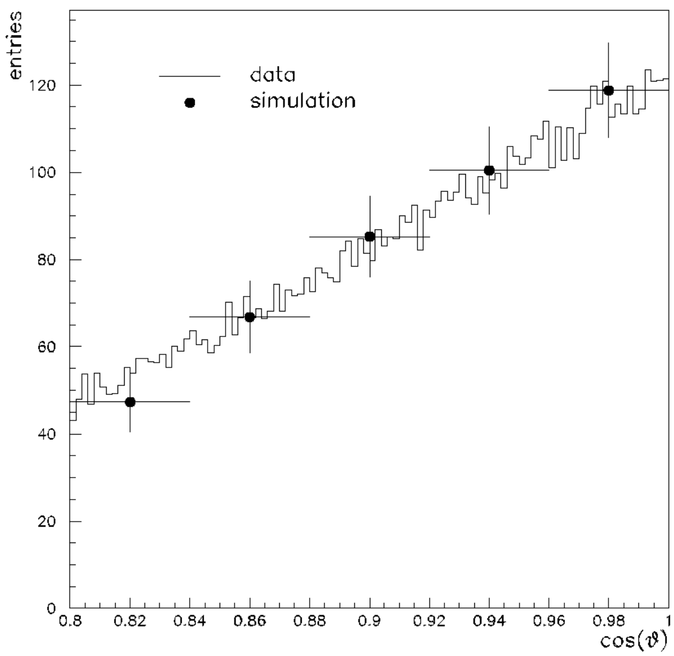


Fig. 22: The zenith angle distribution for data (histogram) and Monte Carlo simulation (points).

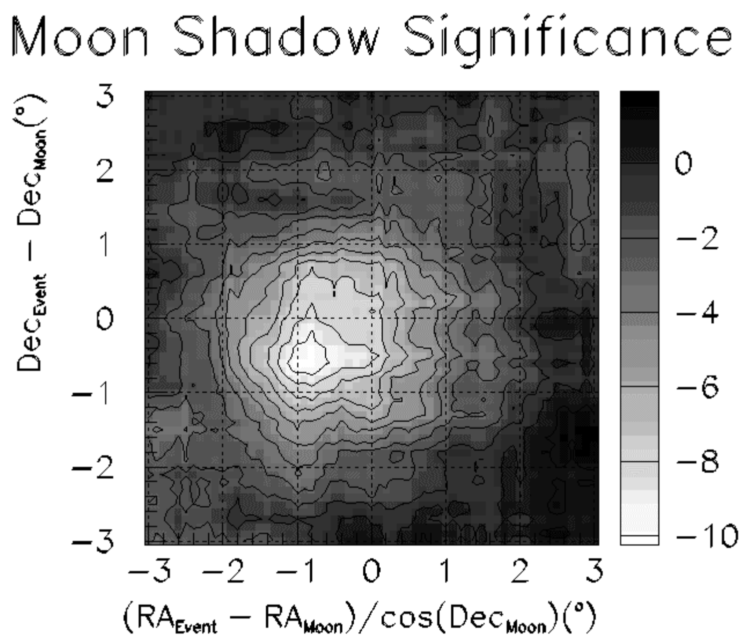


Fig. 23: The shadow of the moon as observed by Milagrito. The actual moon position is at the origin of the figure. The contours are in units of standard deviations (σ) of the event deficit.

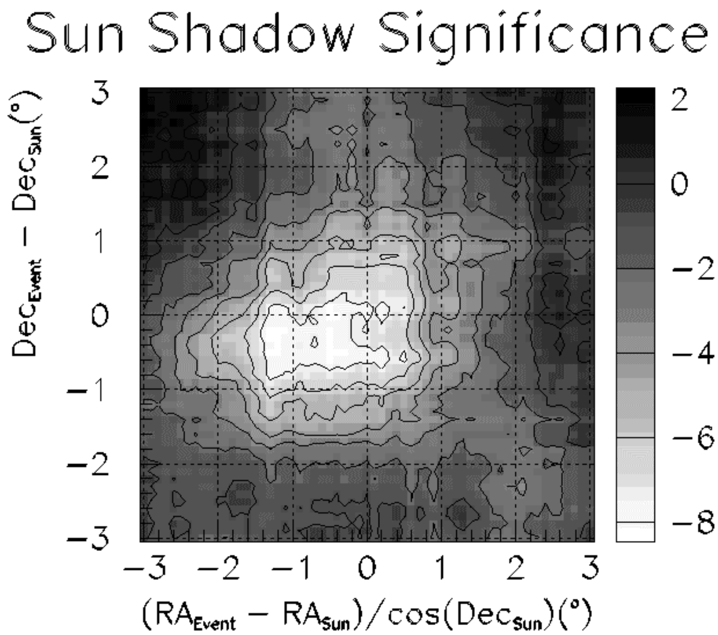


Fig. 24: The shadow of the sun as observed by Milagrito. The actual sun position is at the origin of the figure. The contours are in units of standard deviations (σ) of the event deficit.